Dalton Transactions

ROYAL SOCIETY OF CHEMISTRY

PAPER

View Article Online
View Journal

Cite this: DOI: 10.1039/d5dt02559a

Rhodium porphyrin complexes as catalysts for ammonia borane hydrolytic dehydrogenation

Manuel Minnucci, †[a] Ilaria Barlocco, †[a] Laura Prati, [a] Marta Stucchi, [a] Alberto Villa, [a] Gabriele Di Carlo *[a,b] and Francesca Tessore [a,b]

In this study, we report for the first time rhodium porphyrins as single-site catalysts for the hydrolytic dehydrogenation of ammonia borane (AB), overcoming the traditional role of porphyrin-based materials as stabilizing supports for metal nanoparticles. Rhodium complexes were synthesized by reaction of $RhCl_3 \cdot 3H_2O$ with four free-base porphyrins. To explore homogenous conditions, we chose two cationic (**TMPyP_H$_2$** and **TMAP_H$_2$**) and one anionic (**TSP_H$_2$**) water-soluble core, whereas water-insoluble neutral **TAP_H$_2$** was used as a heterogeneous catalysis. Rhodium porphyrins were fully characterized by UV-vis, ATR-FTIR and NMR spectroscopy, and the content of rhodium was estimated by ICP-MS. Considerably, all the investigated rhodium porphyrins catalyze effectively the hydrolytic dehydrogenation of ammonia borane at 303 K and 1 atm, with varying efficiency. Anionic **TSP_Rh** showed the best performance (70.7% H_2 yield in 9 min, TOF = 15.72 × 10^6 h^{-1}), whereas the two cationic catalysts differed in activity and yield (**TMPyP_Rh**: 68.7% H_2 yield in 7 min, TOF = 3.41 × 10^6 h^{-1}; **TMAP_Rh**: 57.5% H_2 yield in 21 min, TOF = 11.50 × 10^6 h^{-1}). The stability tests pointed out a progressive deactivation of ionic rhodium porphyrins, mainly due to the reaction environment. Indeed, its impact is likely greater on water-soluble complexes, as suggested by a detailed spectroscopic investigation performed on the homogeneous catalysts after use. Conversely, the performances of heterogeneous **TAP_Rh** remained stable over seven successive runs, although the catalyst exhibited lower activity (65.4% H_2 yield in 28 min, TOF = 3.65 × 10^6 h^{-1}). These results strongly demonstrate the efficiency of Rh-based porphyrins as homogeneous and heterogeneous catalysts for the ultra-pure hydrogen production from ammonia borane.

Received 24th October 2025,
Accepted 31st December 2025

DOI: 10.1039/d5dt02559a

rsc.li/dalton

1 Introduction

Fossil fuels have long been the primary energy source worldwide, but their combustion releases hazardous pollutants, contributing to environmental degradation and energy crises. This urgency has driven the search for sustainable and clean energy alternatives, with hydrogen emerging as a promising energy carrier due to its high energy density and near-zero emissions.[1,2] Efficient and safe hydrogen storage is crucial for its practical application, with chemical hydrogen storage being a viable solution, particularly for portable and vehicular applications.[3] Among the various hydrogen storage materials, ammonia borane (AB) stands out for its high gravimetric hydrogen capacity and stability. However, its thermal decomposition requires high temperatures and generates unwanted byproducts, which limit its application. Solvolysis in protic solvents, such as water (hydrolysis) and methanol (methanolysis), provides a more efficient hydrogen release pathway.[4–7] In particular, hydrolysis in the presence of a suitable catalyst facilitates hydrogen generation under mild conditions. The catalytic hydrolysis reaction of ammonia borane can be represented as follows:

$$NH_3BH_3 + 2H_2O \rightarrow NH_4^+ + BO_2^- + 3H_2\ (g)$$

A variety of transition metals have been explored as catalysts for AB solvolysis, with noble metals such as Pt,[8] Rh,[9] Ru,[10] and Pd,[11] as well as non-precious metals like Co,[12] Ni,[13] Cu,[14] and Fe[15] being the most commonly employed. Among such metals, rhodium has attracted particular attention due to its remarkable catalytic activity. The pioneering study by Ramachandran and coworkers[16] first reported the catalytic methanolysis of AB using $RhCl_3$, paving the way for extensive research on rhodium-based catalysts. Following this, numerous studies have focused on rhodium nanoparticles supported on various materials to enhance catalytic performance for hydrogen evolution from AB methanolysis.[17–19] More recently, rhodium-

[a]Dipartimento di Chimica, Università degli Studi di Milano, via Golgi 19, 20133 Milano, Italy. E-mail: gabriele.dicarlo@unimi.it
[b]Consorzio Interuniversitario nazionale per la Scienza e la Tecnologia dei Materiali (INSTM), via Giusti 9, 50121 Firenze, Italy
† These authors equally contributed.

based catalysts have also been extensively investigated for AB hydrolysis under mild conditions, demonstrating exceptional efficiency in facilitating hydrogen release at room temperature.[9,20]

Beyond the use of nanoparticles, researchers have explored various strategies to enhance catalytic efficiency by incorporating metal catalysts into structured frameworks. Among these, porphyrin-based materials have gained significant attention as versatile platforms for metal immobilization. Metal porphyrin-based porous polymers have been synthesized using a solvent-knitting hyper-crosslinked polymer method with tetraphenylporphyrin (TPP) as a building block.[21] These materials exhibit a highly porous structure with ultra-micropores and continuous mesopores, facilitating efficient dispersion of Pd nanoparticles. The resulting Pd-N_4 coordination sites have demonstrated excellent catalytic performance for both AB methanolysis and the hydrogenation of aromatic nitro compounds under mild conditions.[21] Similarly, highly dispersed tetra-(*p*-hydroxyphenyl)porphyrin (THPP)-stabilized Rh, Ru, and Pt nanoparticles have been successfully synthesized for the first time, exhibiting outstanding activity in catalyzing AB hydrolysis for hydrogen evolution.[22] Additionally, hollow framework materials have emerged as promising candidates due to their large surface area, adjustable pore structures, and enhanced mass transport properties. A notable example is the nitrogen-rich hollow porphyrin framework (H-POF), synthesized using SiO_2 as a hard template, which enables the confinement of ultrafine Ni nanoparticles *via* ultrasonic impregnation and reduction. The resulting Ni/H-POF catalyst has demonstrated extraordinary efficiency in promoting the methanolysis of $NaBH_4$, further highlighting the versatility of porphyrin-based frameworks for hydrogen generation applications.[23] These advances in porphyrin-based catalysts underscore their potential as robust and tunable platforms for metal immobilization, offering new pathways for optimizing catalytic performance in AB decomposition.

Indeed, porphyrins have generally emerged as highly promising materials in sustainable energy applications due to their unique electronic properties and catalytic versatility. These macrocyclic organic compounds, with their extended π-electron conjugation, have been widely studied in fields such as catalysis,[24,25] optoelectronics,[26–28] photovoltaics,[29–31] and artificial photosynthesis.[32–34] Their structural flexibility, combined with their ability to mediate charge transfer and energy conversion, makes them valuable tools for advancing hydrogen storage and generation technologies by AB hydrolytic dehydrogenation.

Over the last few decades rhodium porphyrins have become archetypal organometallic scaffolds because they are easy to prepare and their oxidation states can be tuned with remarkable precision.[35] Early work showed that Rh(III) porphyrins, obtained by straightforward metalation of free-base macrocycles, behave as strong electrophiles, mediating sp^2-C–H alkylation and anti-Markovnikov alkene hydration. Reduction with hydrogen or hydride reagents[36–39] converts these Rh(III) species into square-planar, nucleophilic Rh(I) complexes, which in turn serve as gateways to Rh(II) metalloradicals. The latter are normally isolated as Rh–Rh dimers, but can persist as monomeric radicals when bulky meso- or β-substituents block dimerization. Equipped with a half-filled d_{z^2} orbital, Rh(II) porphyrins display striking radical chemistry: they split H_2, cleave otherwise inert sp^3 C–H bonds, and even open unstrained β-C–C bonds through rare termolecular transition states. Pioneering studies by Chan and co-workers have since extended these reactivities to catalytic C–C scission and to the hydration of alkenes and alkynes,[40,41] underscoring that the full catalytic potential of Rh-porphyrins is only beginning to be realized.

Structurally, the rigid, near-planar porphyrin ring offers a highly aromatic, inward-oriented N_4 pocket that locks rhodium into square-planar, square-pyramidal, or octahedral environments depending on its oxidation state. Steric loading at the meso or β positions (*e.g.*, mesityl groups) puckers the macrocycle and sterically "shields" the metal, slowing ligand exchange yet stabilizing monomeric Rh(II) radicals. Conversely, less hindered macrocycles such as tetraphenylporphyrin (TPP) grant easier access to metal-centered substitution and favour Rh–Rh dimer formation. The resulting platform stabilizes Rh(I), Rh(II), and Rh(III) equally well, enabling a broad palette of redox-driven transformations.

Catalytically, rhodium porphyrins first drew attention in reductive chemistry when Aoyama and co-workers showed that Rh(III) porphyrins catalyze the $NaBH_4/O_2$ reduction of ketones *via* borane transfer, one of the earliest demonstrations of metalloporphyrins promoting borane chemistry under aerobic conditions.[42] Yet, despite this precedent and the extensive C–H/C–C activation chemistry just described, rhodium porphyrins have scarcely been explored for hydrogen generation. To date, only Rh-porphyrin-stabilized nanocomposites, rather than single-site molecular complexes, have been evaluated for ammonia-borane (NH_3BH_3) hydrolysis, giving modest turnover frequencies (*ca.* 214 mol H_2 mol^{-1} min^{-1}).[22] Single-site rhodium porphyrins as homogeneous or heterogeneous catalysts for AB hydrolysis therefore remains an open and promising frontier.

Building upon this background, we present the first example of ammonia borane hydrolysis catalyzed by four distinct rhodium porphyrin complexes, employed as single-site catalysts in both homogeneous and heterogeneous systems (Chart 1).

For homogeneous catalysis, we focused on three water-soluble ionic porphyrins: two cationic derivatives, 5,10,15,20-Tetrakis(4-trimethylammoniophenyl)porphyrin (**TMAP_H_2**) and 5,10,15,20-(tetra-*N*-methyl-4-pyridyl)porphyrin (**TMPyP_H_2**), along with the anionic 5,10,15,20-(tetra-4-sulfonatophenyl)porphyrin (**TSP_H_2**). The choice of these porphyrins allowed us to investigate how their different charge distributions and electronic properties may affect the catalytic efficiency. For heterogeneous catalysis, we employed the neutral 5,10,15,20-(tetra-4-aminophenyl)porphyrin (**TAP_H_2**), which, due to its water-insolubility, provides a stable and recoverable catalytic system.

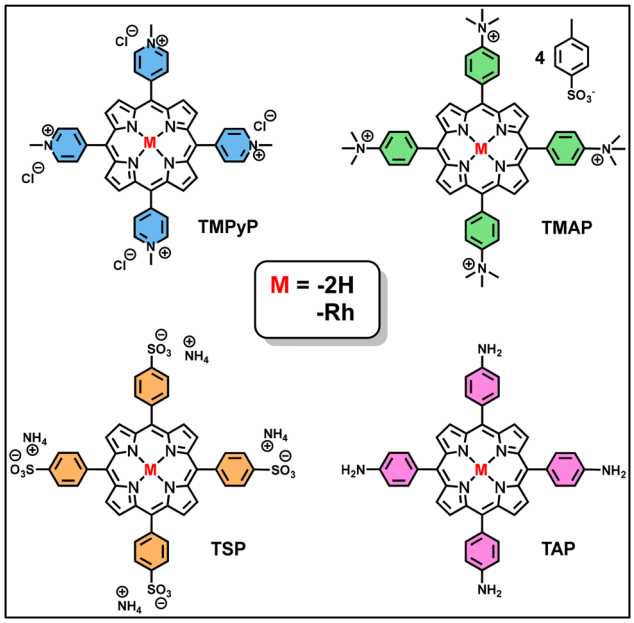

Chart 1 Molecular structures of the investigated porphyrins.

2 Results and discussion

2.1 Rh(III) porphyrin complexes: synthesis and spectroscopic characterization

All rhodium catalysts were easily and readily obtained by metalation of the selected free-base porphyrins. While the cationic **TMAP_H$_2$** and **TMPyP_H$_2$**, along with the neutral **TAP_H$_2$**, were sourced commercially, the anionic porphyrin **TSP_H$_2$** was synthesized following a modified literature procedure,[43,44] from commercially available TPP_H$_2$. The porphyrin was combined with concentrated H_2SO_4 to form a thick paste, which was heated at 140 °C for 6 h and then allowed to cool to room temperature overnight. Ice-cold water was added slowly, precipitating a green solid that was separated from the acidic supernatant by centrifugation. The precipitate was washed three times with water, dissolved in methanol to give a dark-green solution, and treated dropwise with 7 N methanolic NH_3 until a red solid formed. Filtration and thorough methanol washing afforded $[TSP\_H_2]^{4-}\cdot 4NH_4^+$ in 93% yield.

Several methods have been developed to optimize the coordination of various porphyrin cores with rhodium ions, resulting in stable and functional metal–ligand complexes.[35,45] Key factors such as solvent choice, reaction conditions, and stoichiometry have been extensively studied to maximize yield and product purity. Among the tested solvents, dimethylformamide (DMF) is considered the most effective for facilitating metalation.[35,46–48] Herein, a solution of $RhCl_3\cdot 3H_2O$ (2.0 equivalents) in DMF was refluxed for 30 minutes until a yellowish solution was obtained. The appropriate free-base porphyrin (1.0 equivalent) dissolved in ethanol was then added dropwise, and the reaction mixture was refluxed for an additional 24 hours. After completion of the reaction, the solvents were evaporated under reduced pressure. The water-soluble ionic porphyrins were first purified by passing the residues through alumina with aqueous NaOH (pH about 10) while **TAP_Rh** with DMF. Then the crude products were further purified by Celite plug filtration with proper solvents. Finally, **TMPyP_Rh** and **TAP_Rh** were recovered as solid by filtration from their acetone dispersion, while the hygroscopic **TSP_Rh** and **TMAP_Rh** derivatives were finally obtained by freezing the aqueous filtrate followed by lyophilization.

Reaction progress was followed by ^{1}H NMR, changes in the UV-visible and ATR-FTIR spectra, and fluorescence quenching. Characterizing rhodium porphyrins, particularly the ionic derivatives, is non-trivial: once metalated, these macrocycles become markedly less soluble than their free-base analogues; the rhodium center can exhibit various oxidation states and adopt an octahedral structure with two axial ligands whose identity depends strongly on medium and conditions; and ionic substituents make spectroscopic measurements sensitive to ionic strength, counter-ions, and solution pH. When DMF is used for metalation at elevated temperature it can decompose, supplying dimethylamine that binds axially to the newly formed rhodium porphyrin.[46–49] In water, however, the axial sites are labile and are rapidly replaced by solvent to give bis-aquo or, at higher pH, hydroxo species.[39] All rhodium complexes were analyzed by ^{1}H NMR in appropriate deuterated solvents (THF-d_8 for **TAP_Rh** and D_2O for the water-soluble ionic derivatives). In every case the characteristic inner N–H resonance at ≈−3 ppm vanished, while new upfield signals corresponding to axially bound solvent appeared, confirming successful metalation. Reaction progress was also checked by thin-layer chromatography, using C18 reverse-phase TLC with EtOH/H_2O for the water-soluble complexes, and silica-gel TLC with DCM/MeOH for the insoluble **TAP_Rh** analogue. Relative to the free-base porphyrins, the rhodium complexes showed altered R_f values and complete fluorescence quenching, further verifying that the metalation was complete.

To further confirm the coordination of rhodium in the cavity of the porphyrins, ATR-FTIR was employed (Fig. 1).

Due to the complex nature of the molecules, a detailed interpretation of the IR spectrum is challenging. In any case, some valuable insights into the N–H absorption regions were provided, *i.e.* at wavenumbers > 3000 cm^{-1} for stretching and 1650–1580 cm^{-1} for bending. A sharp peak around 1419 cm^{-1} and a medium band at 1595 cm^{-1} are assigned to N–H bending and C–N stretching vibrations, respectively. These signals overlap with the C=C stretching vibrations of the phenyl ring and are influenced by the presence of the metal.[43,50] The presence of an N–H bond in the starting porphyrins is confirmed by the IR band observed in the 3300–3400 cm^{-1} region, corresponding to N–H stretching vibration. Notably, rhodium porphyrins do not exhibit any N–H stretching absorption, which is present in the metal-free porphyrin.[51] This band was monitored to track the insertion of rhodium into the porphyrin core. Additionally, a broad, medium-intensity peak at 3436 cm^{-1} can also be attributed to the overlapping O–H stretching vibration of absorbed water.

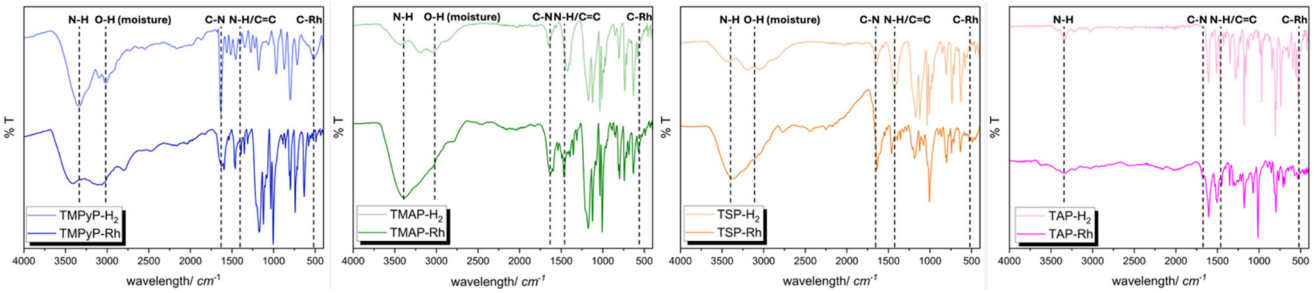

Fig. 1 Synopsis of the FTIR-ATR spectra of free-base and Rh(III) porphyrins.

This effect is particularly relevant due to hygroscopic nature of the catalyst, especially in the presence of sulfonated and ammonium groups in anionic and cationic porphyrins.[43,52] Upon complexation, a medium-intensity absorption at 560 cm^{-1} appears in the IR spectrum, which is attributed to the Rh–C stretching vibration, further confirming the coordination of rhodium.[50,51]

Another tool to track porphyrin complexation is UV-Vis absorption spectroscopy which offers valuable information on metal coordination, structural changes, and the aggregation behavior of the derivatives.[53,54] To assess the effect of metalation, we compared the UV-Vis absorption spectra of the free-base porphyrins with those of their corresponding Rh(III) complexes (Fig. 2 and Fig. S1–S7). For the ionic species, spectra were recorded in water across a concentration range of 1.0×10^{-4} to 5.0×10^{-7} M to evaluate adherence to the Lambert–Beer law (Fig. S1–S6). In contrast, the spectra of the neutral **TAP_H$_2$** and **TAP_Rh** were measured in THF; however, due to the limited solubility of **TAP_Rh** in this solvent, a full multi-concentration analysis was not feasible. A summary of the experimental results is provided in Table 1.

The UV-Vis absorption patterns of all porphyrins are in accordance with the "four orbital model" proposed by Gouterman.[54,55] Free-base porphyrins show one intense ($\varepsilon \approx 10^5$ M^{-1} cm^{-1}) B band at 410–430 nm and four weaker ($\varepsilon \approx 10^3$–10^4 M^{-1} cm^{-1}) Q bands at higher energies (500–660 nm).

All the bands are assigned to HOMO–LUMO $a_{1u}(\pi)$,$a_{2u}(\pi) \rightarrow e_g(\pi^*)$ porphyrin-ring-based electronic transitions.[56] The B band arises from a $S_0 \rightarrow S_2$ transition, whereas the Q bands are due to $S_0 \rightarrow S_1$ ones. The lowering of the number of Q bands

Table 1 Synopsis of the experimental UV-Vis data

Compound	B band λ_{max} (nm)	B band log ε	Q band λ_{max} (nm)	Q bands log ε
TMPyP_H$_2$	422	5.31	518, 554, 584, 638	4.14, 3.70, 3.77, 3.07
TMPyP_Rh	417	5.21	529, 562	4.13, 3.40
TMAP_H$_2$	412	5.63	514, 550, 579, 634	4.22, 3.74, 3.79, 3.46
TMAP_Rh	415	5.12	527, 560	4.13, 3.32
TSP_H$_2$	413	5.56	516, 550, 580, 633	4.03, 3.76, 3.73, 3.59
TSP_Rh	424	4.73	534, 566 (sh)	3.86
TAP_H$_2$	430	5.42	524, 568, 662	4.22, 4.07, 3.88
TAP_Rh	437		542, 585	

with the disappearance of those above 580 nm proves the coordination of Rh(III) to the pyrrolic nitrogen atoms, which increases the molecular symmetry from D_{2h} to D_{4h}. Moreover, complexation induces a decrease of the intensity of the absorption bands as confirmed by the diminished molar absorption coefficient of metal-porphyrins.

While UV-Vis absorption readily confirms complexation at first glance, a more detailed analysis can also provide valuable insights into additional aspects of the system. Rhodium complexation generally induces a hypsochromic (blue) shift in the B bands of porphyrins. However, in the presence of strongly coordinating solvents such as pyridine or DMF, a bathochromic (red) shift in the absorption spectrum may occur instead.[53] Additionally, the aggregation behavior of porphyrins can significantly influence their spectral features: the formation of H-aggregates (head-to-head arrangement) typically leads to a blue shift of the B bands, whereas J-aggregates (head-to-tail) result in a red shift of the same transitions.

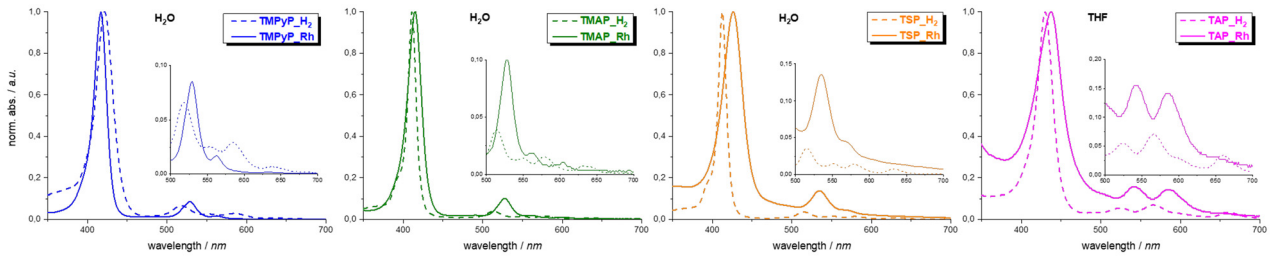

Fig. 2 Normalized UV-Vis absorption spectra of free-base and Rh(III) porphyrins investigated in this work. Insets show an enlargement of the Q band zone.

The spectroscopic comparison of ionic porphyrins and the neutral one in diluted solution deserves a separate discussion. The UV-Vis spectra of the water-soluble porphyrins TMAP, TMPyP, and TSP, both in their free-base and metalated forms, were recorded in dilute aqueous solution at pH 7. Under these conditions, it is well established that the predominant rhodium–porphyrin species in solution are bis-aquo complexes, as supported by numerous literature reports,[37–39] thus any influence from variations in coordinated solvents can be ruled out for these species. However, in a previous study, Golovina and Vasil'ev demonstrated that while the cationic rhodium complexes **TMAP_Rh** and **TMPyP_Rh** remain monomeric in aqueous solution, the anionic **TSP_Rh** tends to dimerize, forming a head-to-tail aggregate.[56] Accordingly, the absorption spectrum of **TMPyP_Rh** shows a sharper and blue-shifted B-band relative to its free-base counterpart, consistent with rhodium complexation occurring in a monomeric form. In the case of **TMAP_Rh**, the B-band is nearly superimposable with that of **TMAP_H$_2$**, exhibiting only slight broadening and a modest red shift, suggesting the complex predominantly exists as a monomer, with a minor contribution from J-aggregates. In contrast, the spectrum of **TSP_Rh** displays a significantly broadened and red-shifted B-band compared to its free-base analogue, indicating a higher degree of aggregation, likely due to head-to-tail dimer formation. Similar to **TSP_Rh**, the complexation of the water-insoluble **TAP_H$_2$** results in an absorption spectrum in dilute THF characterized by a broadened and red-shifted B-band, consistent with the formation of J-aggregates, an expected outcome for a molecule with such limited solubility in most solvents.

2.2 Catalytic tests

Following confirmation of successful metalation, the rhodium content in each complex was quantified by ICP-MS analysis (Table 2). This step is essential to accurately normalize the catalytic performance of the catalysts based on their actual rhodium loading.

The selected rhodium porphyrin complexes were used as catalysts in the hydrolysis of ammonia borane. Firstly, the precursor employed to metalate the porphyrins ($RhCl_3{\cdot}3H_2O$) was tested at the same reaction conditions, to exclude its role in the catalytic activity and underlying the importance of the porphyrin core. Fig. S7 shows the kinetic profile of this specie. Indeed, after an initial considerable activity, it poisons reaching the plateau after only 37 seconds (H_2 yield of 14%). Specifically, the three ionic, water-soluble porphyrins (**TMPyP_Rh**, **TMAP_Rh**, and **TSP_Rh**) were chosen for evaluation as homogeneous catalysts, while the neutral **TAP_Rh** complex was prepared and applied as a heterogeneous catalyst, enabling a comparative study of their catalytic performances across different environments.

Table 2 H_2 yield, end of the reaction time and TOF for the different catalysts tested in the hydrolytic AB decomposition

Catalyst	Yield H_2/%	Time/min	TOF/h^{-1} 10^6	%Rh (ICP)
TMPyP_Rh	68.7	7	3.41	10.30 ± 0.08
TMAP_Rh	57.5	21	11.50	4.80 ± 0.12
TSP_Rh	70.7	9	15.72	11.80 ± 0.41
TAP_Rh	65.4	28	3.65	12.70 ± 0.64

The materials were tested in a batch reactor under mild reaction conditions (303 and 1 atm). The hydrogen evolution was monitored by the Men On the Moon kit, measuring the partial pressure of the products evolved.

The kinetic profiles were collected until the end of the reaction, indicated by a pressure plateau. Fig. 3 shows the time evolution of H_2 production normalised on the initial moles of AB (nH_2/nAB_0) for the homogeneous catalysts, *i.e.* **TMPyP_Rh**, **TMAP_Rh** and **TSP_Rh**. It is worth noting that none of the catalysts evaluated produces the maximum theoretical equivalents of H_2, likely due to the incomplete decomposition of ammonia borane. The anionic porphyrin, **TSP_Rh**, showed the best catalytic performance, with a TOF of 15.72×10^6 h^{-1} and a 70.7% hydrogen yield in only 9 minutes (Table 2). The two cationic catalysts showed a very different catalytic behaviour. Indeed, **TMPyP_Rh** reached a 68.7% H_2 yield in 7 minutes after almost one minute of activation time, which can be observed from the sigmoidal shape and the relatively low TOF (3.41×10^6 h^{-1}) (Fig. 3 and Table 2). It is worth mentioning that using **TMPyP_Rh** a sigmoidal shape was observed in the first run. This kinetic profile, described by a Finke–Watzky kinetic model,[57,58] is typically indicative of a transformation or reconstruction within the active phase, evolving from a metastable to a more stable state. Recently, we demonstrated that this stable active phase is not necessarily the reduced metal. In that study, we showed that the support itself undergoes reduction, thereby altering the electronic and redox properties of the active phase.[59] Moving from **TMPyP_Rh** to **TMAP_Rh** porphyrin the activity largely increases with a hydrogen productivity of 11.50×10^6 h^{-1}, but giving a lower H_2 yield (57.5%) in a longer time, 21 minutes. It is important to highlight that, despite variations in their catalytic performance, all the synthesized rhodium porphyrin complexes function effectively as single-site catalysts for ammonia borane hydrolysis. To the best of our knowledge, these represent the first reported examples of rhodium porphyrins applied directly to this transformation. Another important parameter to establish the overall performance and applicability of a catalyst is its stability over numerous reaction runs. Indeed, we performed recyclability tests over all the different employed systems by adding the same amount of ammonia borane after the end of the reaction, without separating the catalyst from the reaction environment. So, after reaching the pressure plateau the system was open and closed. After the equilibrium was reached, 400 μL of a 1 M ammonia borane aqueous solution was injected at once and the reaction profile was monitored.

Starting from the best performing porphyrin, **TSP_Rh**, in Fig. 3, we could observe a gradual deactivation in terms of activity over the five consecutive runs performed, while the H_2 selectivity remains almost constant. **TMPyP_Rh** and **TMAP_Rh** showed a similar behaviour in terms of TOF, but an increase in the H_2 yield was observed over all the stability runs.

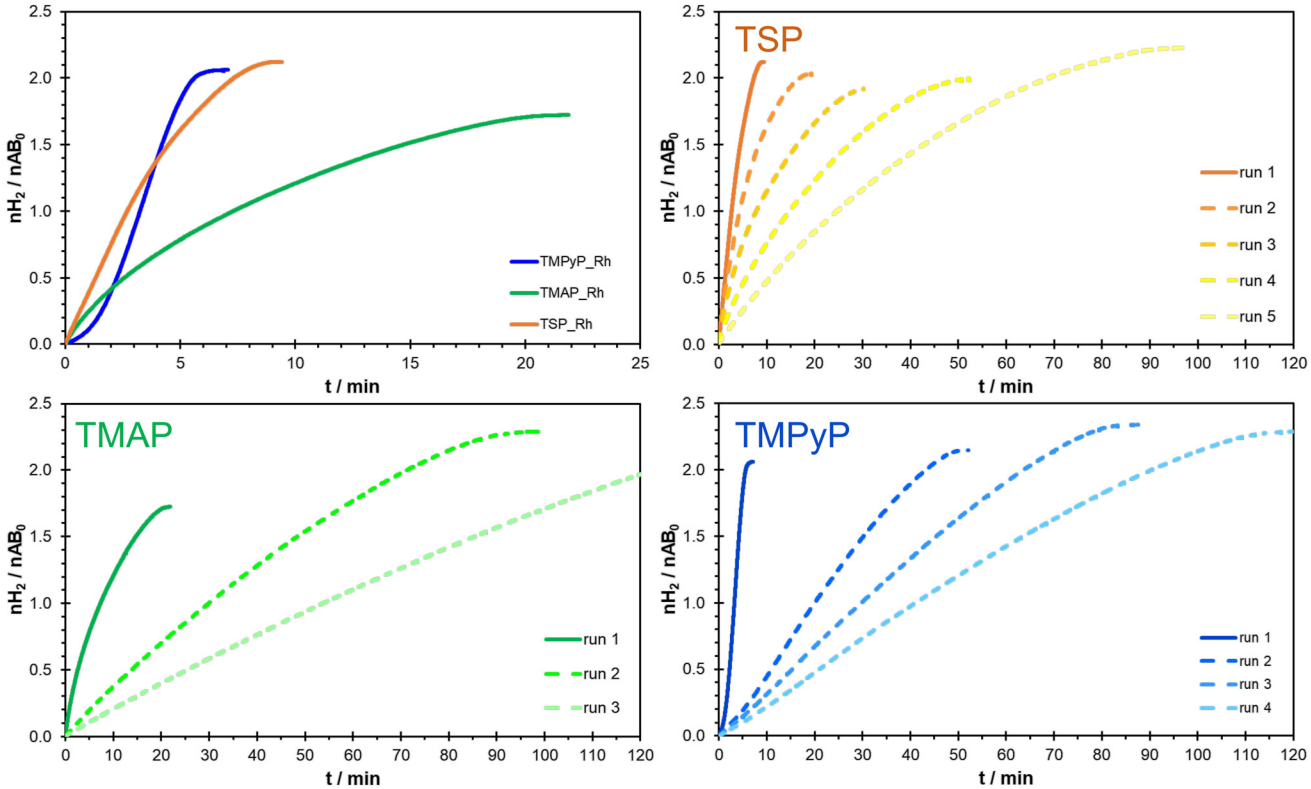

Fig. 3 Kinetic profiles and reusability tests of the homogeneous porphyrins for ammonia borane hydrolysis. All tests were performed at least three times at 303 K and 1400 rpm using a 7.4×10^{-2} M AB solution.

To implement the poor stability of homogeneous rhodium porphyrins in ammonia borane dehydrogenation, the neutral **TAP_Rh** porphyrin, functioning as a heterogeneous catalyst in aqueous environment, was employed (Fig. 4). This complex achieved a hydrogen yield of 65.4% within 28 minutes, corresponding to a TOF of 3.65×10^6 h^{-1}.

As expected, the stability tests conducted under heterogeneous conditions with **TAP_Rh** yielded markedly different results compared with the homogeneous porphyrins. Although the catalyst exhibited lower activity during the initial run, its performance remained consistent over seven successive cycles, with a gradual increase in hydrogen production yield observed across the repeated tests (Fig. 4). These differences can be attributed to the aqueous reaction environment, which likely has a greater impact on the water-soluble ionic porphyrins than on their neutral counterparts. It is important to consider that during the catalytic process, the pH of the solution gradually increases, passing from 5 to 10, as a result of the formation of the weakly basic BO_2^- species generated from the decomposition of ammonia borane, affecting especially the homogeneous catalysts and leading to different results in terms of activity and stability.

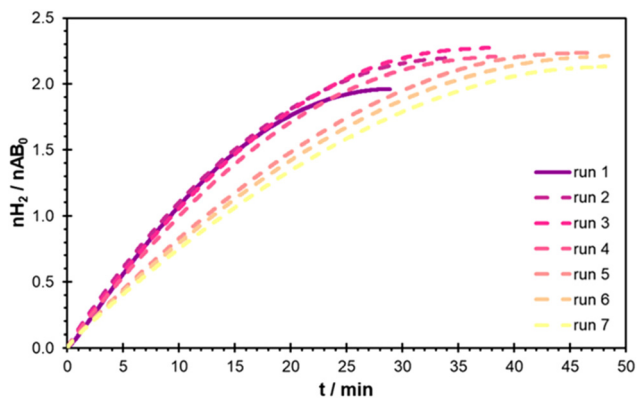

Fig. 4 Kinetic profiles of the **TAP_Rh** for ammonia borane hydrolysis. All tests were performed at least three times at 303 K and 1400 rpm using a 7.4×10^{-2} M AB solution.

2.3 Spectroscopic investigation of the catalysts after use

To better understand the influence of the aqueous environment on the water-soluble ionic catalysts, a comprehensive spectroscopic study was conducted on the best performing homogeneous catalyst, *i.e.* **TSP_Rh**. This included monitoring changes in the UV-Vis absorption profiles of the rhodium porphyrins following the first catalytic cycle, as well as under varying pH conditions.

Additionally, the catalysts were subjected to hydrogenation treatments, either by exposure to H_2 gas (under 2 bar for 2 hours) or by reaction with $NaBH_4$, and the resulting spectral changes were analyzed and compared. To further assess poten-

tial changes in axial coordination and evaluate all the different ligands that can interact with the catalysts and ionic strength during catalysis, $NaBO_2$ was also introduced into the solution and its effects on the absorption spectra were evaluated. First, we recorded the absorption spectra of the aqueous reaction mixtures of **TSP_Rh** after the first catalytic run, both in deionized water (pH 7) and in ammonium buffer solution (pH 10), and compared them with the spectrum of the catalyst in water prior to catalysis (Fig. 5). Notably, following the catalytic run, the spectrum of **TSP_Rh** in deionized water (pH 7) exhibited significant changes compared to the pre-catalysis profile (Fig. 5a). The B-band became markedly sharper and showed a hypsochromic shift of approximately 10 nm. Additionally, the Q-band region underwent substantial modification: whereas only a single Q-band at 535 nm was visible before catalysis, two distinct Q-bands appeared after the reaction, including a new band at 600 nm with intensity comparable to that at 535 nm. However, when the post-catalysis **TSP_Rh** sample is diluted in ammonium buffer at pH 10, the spectral profile undergoes broadening and a red shift of the B-band, along with a simplification of the Q-band region. The resulting spectrum closely resembles that of **TSP_Rh** prior to catalysis, except for two additional low-intensity Q-bands barely perceptible at 570 and 613 nm. The sharp and blue-shifted B-band observed in the spectrum after catalysis at pH 7 indicates that the active species during the first catalytic run likely exists in a monomeric form. The emergence of a second, intense Q-band at 600 nm suggests that the rhodium center is no longer strictly confined to a square-planar geometry, but instead adopts a "sitting-atop" (SAT) configuration.[60,61] This distortion is likely due to the coordination of a strongly interacting axial ligand, which slightly displaces the rhodium center out of the porphyrin plane. However, we cannot exclude the possibility that the observed spectral features arise from the formation of a catalytic intermediate in a reduced Rh(I) oxidation state, such as $[TSP\_Rh^{I}(H_2O)]^{5-}$, potentially adopting a square-pyramidal, five-coordinate geometry. Alternatively, the formation of a hydride species like $[TSP\_Rh(H)(H_2O)]^{4-}$ could also account for the observed asymmetry, as it would disrupt the molecular symmetry of the complex. However, this active species appears to be stable only under neutral or mildly basic conditions. As the basicity increases, such as after multiple catalytic cycles, it likely transforms into a less active and less soluble aggregated form. This is supported by the observed decline in catalytic activity over successive runs, the broadening of the B-band in the absorption spectrum at pH 10, and the visible formation of a precipitate in the reaction medium during the stability tests.

To rule out the possibility that the observed spectral changes are due to the formation of hydroxo species (such as the mono-hydroxo complex $[TSP\_Rh^{III}(H_2O)(OH^-)]^{4-}$ or the dihydroxo complex $[TSP\_Rh^{III}(OH^-)_2]^{5-}$) under basic conditions, we also recorded the absorption spectra of the rhodium complex before catalysis in both pH 7 and pH 10 aqueous solutions. The resulting spectra were completely superimposable (Fig. S9), indicating that neither the conversion from the bis-aqua complex $[TSP\_Rh^{III}(H_2O)_2]^{3-}$ at pH 7 to the hydroxo forms at pH 10 produces any significant spectral differences.

Wayland *et al.* demonstrated that low oxidation state species such as $[TSP\_Rh^{I}(H_2O)]^{5-}$ or $[TSP\_Rh(H)(H_2O)]^{4-}$ can be generated by reducing the bis-aquo Rh(III) complex using hydrogen gas or a chemical reductant like $NaBH_4$.[39] Based on this, the **TSP_Rh** complex was subjected to reduction either by exposure to pressurized hydrogen for 2 hours or by treatment with $NaBH_4$.

The resulting absorption spectra were recorded under acidic (acetic acid/acetate buffer 0.1 M), neutral, and basic (ammonium buffer 0.1 M) conditions and subsequently compared (Fig. S10). In all cases, the spectra were nearly identical to that of the post-catalysis complex at pH 10, displaying the same additional low-intensity Q-bands at 570 and 613 nm. Therefore, we can reasonably conclude that the active species formed during the first catalytic cycle is not identical to the

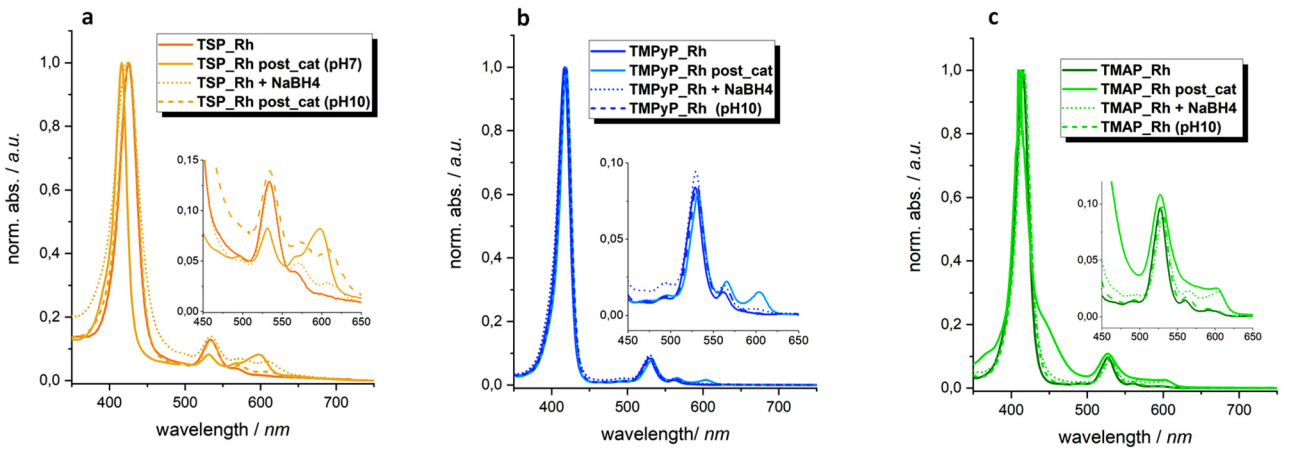

Fig. 5 UV-Vis spectra of (a) TSP-Rh, (b) **TMPyP_Rh** and (c) **TMAP_Rh** before and after the first catalytic run, varying the pH and after addition of $NaBH_4$.

reduced forms generated by treatment with hydrogen or $NaBH_4$. Instead, it appears that the complex gradually converts into the reduced species as the basicity of the solution increases. By exclusion, we propose that the active species is a transient intermediate, likely formed *in situ* during the course of the ammonia borane hydrolysis reaction, and not readily accessible through direct chemical reduction. Additional experiments were carried out by recording the absorption spectra of **TSP_Rh** in an aqueous solution of $NaBO_2$ (0.1 M) to evaluate any effects induced by the increasing concentration of BO_2^- during catalysis (Fig. S10). The resulting spectrum was nearly identical to that of the catalyst in pure water, showing only a slight bathochromic shift (approximately 3 nm) across all bands. This minor shift is likely attributed to the increased ionic strength of the solution rather than a direct interaction between the BO_2^- anion and the rhodium center.

A similar spectroscopic investigation was conducted for the **TMAP_Rh** and **TMPyP_Rh** catalysts (Fig. 5b and c). In both cases, the emergence of an additional intense Q-band around 600 nm was observed after the first catalytic run. However, unlike **TSP_Rh**, the cationic porphyrins remain in monomeric form under all tested conditions, with no noticeable broadening of the absorption bands at basic pH. Notably, the slower reduction kinetics of **TMAP_Rh** upon reaction with $NaBH_4$ enabled us to track the evolution of its spectral features over time (Fig. S11). Five minutes after $NaBH_4$ addition, the B-band showed a marked hypsochromic shift, and the Q-region displayed multiple prominent bands at 500, 533, 570, and 603 nm. From 15 minutes to 60 minutes, the spectrum progressively evolved into the profile observed following the first catalytic run. These observations strongly support the formation of a transient active intermediate during the reaction, which is difficult to isolate, but can be spectroscopically captured during its evolution.

Numerous mechanisms for ammonia borane hydrolysis have been proposed in literature, primarily involving supported metal catalysts. However, to the best of our knowledge, no mechanistic studies have been reported to date for AB hydrolysis catalyzed by rhodium-porphyrin as single-site complexes. While we cannot rule out the involvement of rhodium-based intermediates in lower oxidation states (such as Rh(I), rhodium hydride (Rh–H), or even Rh(II)) and acknowledge that a more detailed investigation is required, we tentatively propose hereafter a preliminary mechanism aligned with existing studies. This mechanism involves the formation of an active intermediate complex between the rhodium porphyrin and ammonia borane, which then facilitates AB hydrolysis by promoting its decomposition through a coordinated activation pathway (Scheme 1).

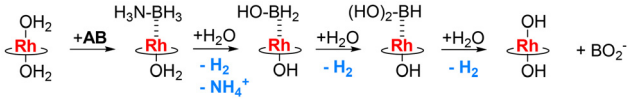

Scheme 1 Proposed mechanism for hydrogen evolution from hydrolytic dehydrogenation of ammonia borane.

3 Experimental

TAP_H$_2$ and 5,10,15,20-(tetraphenyl)porphyrin (TPP_H$_2$) for the synthesis of **TSP_H$_2$** were puchased from Porphychem, whereas **TMAP_H$_2$**, $RhCl_3{\cdot}3H_2O$ and ammonia borane (AB, NH_3BH_3, 90%)from Merck. **TSP_H$_2$** was prepared optimizing a literature method.[43,44] UV-Vis electronic absorption spectra of ionic porphyrins, both free-base and metal complexes, were recorded at room temperature in H_2O while tetrahydrofuran (THF) was used for **TAP_H$_2$** and **TAP_Rh** using a Shimadzu UV3600 spectrophotometer and quartz cuvettes with 1 cm optical path length. ^{1}H-NMR spectra were recorded on a Bruker Avance DRX-400 in D_2O or THF-d_8 (Cambridge Isotope Laboratories, Inc.). ATR-FTIR spectra were acquired on a PerkinElmer Frontier instrument equipped with an ATR accessory with a diamond/ZnSe crystal. The IR spectra were collected in the range 4000–400 cm^{-1}. Lyophilization was carried out on a Freeze Dryer CoolSafe 55-4 (LABOGENE). ICP-MS analyses were performed on an Agilent 7850 ICP-MS, using for calibration an Agilent IMS-103 calibration standard. Elemental analysis was carried out with a PerkinElmer CHN 2400 instrument.

The hydrolytic dehydrogenation of AB was performed in a 27 mL two-necked round bottom flask at a constant reaction temperature of 303 K. Hydrogen evolution was followed by using the Man On the Moon X104 kit, monitoring the partial pressure of the released product.[62–64] Usually, the selected amount of catalysts (AB/Rh molar ratio 1000/1) is added to the reactor containing 5.0 mL of distilled water and the desired temperature is reached. This was connected with a switchable three-way valve through a Torion screw. Then, the valve was switched to the pressure transducer which is connected *via* wireless to the software recording the kinetic profile online. When the equilibrium was reached indicated by a stable pressure value, 0.4 mmol of AB were injected and stirred at 1400 rpm, starting the reaction. The kinetic profiles were collected until the reaction end, indicated by the pressure plateau and collecting 0.5 points per s. To confirm the reproducibility of the experiments, catalytic tests were repeated at least three times. The turnover frequency (TOF) was calculated as the slope of the initial kinetic profile (between 0 and 1.5 minutes) normalized for the employed moles of metal (based on ICP results).

4 Conclusions

In the present work we developed the first examples of rhodium porphyrins as single-site catalysts for the hydrolytic dehydrogenation of ammonia borane in aqueous media under mild conditions. We considered three ionic water-soluble porphyrins (anionic **TSP_H$_2$**; cationic **TMPyP_H$_2$** and **TMAP_H$_2$**) for homogeneous catalysis, and one water-insoluble neutral core (**TAP_H$_2$**) to explore heterogeneous conditions. We pre-

pared the corresponding rhodium complexes by reaction of the free-bases with $RhCl_3{\cdot}3H_2O$, and we fully characterized them by UV-Vis, ATR-FTIR and NMR spectroscopies. The metal loading was measured by ICP-MS. Then, we tested our catalysts in a batch reactor at 303 K and 1 atm.

Considerably, all the investigated rhodium porphyrins catalyzed ammonia borane hydrolysis efficiently, with some differences in their performances. The best results were achieved by anionic **TSP_Rh**, which led to high values of H_2 yield and TOF in a few min. On the other hand, the two cationic catalysts showed lower H_2 yields and TOFs. In particular, **TMAP_Rh** appeared more active than **TMPyP_Rh**, but produced a lower H_2 yield in a longer time. We performed stability tests on the three ionic complexes, which pointed out an increasing deactivation of the catalysts. Conversely, the performance of heterogeneous **TAP_Rh** catalyst remained consistent over seven successive cycles with a gradual increase in H_2 production yield across the repeated tests, despite the lower activity displayed during the initial run.

To delve deeper into the understanding of the catalytic behavior of our ionic rhodium porphyrins in an aqueous environment, we conducted a comprehensive spectroscopic investigation on **TSP_Rh** after the first catalytic cycle, as well as on pristine **TSP_Rh** varying pH, exposing it to gaseous H_2, or adding $NaBH_4$ or $NaBO_2$. The UV-Vis absorption profiles strongly suggested the presence of an active species gradually formed *in situ* during the first catalytic run, which cannot be generated by direct reaction of pristine **TSP_Rh** with H_2, $NaBH_4$ or $NaBO_2$. This active species is likely a monomeric form of the catalyst, with the rhodium center in a sitting atop configuration due to axial ligand coordination, as also supported by the similar spectroscopic investigation on **TMAP_Rh** and **TMPyP_Rh**. This study paves the way to the use of Rh porphyrins in hydrogen production from ammonia borane. Further investigations will be performed in the near future to further optimize the catalyst and to have insight into the deep understanding of the whole reaction mechanism.

Author contributions

Conceptualization: G. D. C., A. V. and F. T.; formal analysis: M. M. and I. B.; investigation: M. M. and I. B.; supervision: G. D. C., A. V., F. T. and L. P.; visualization: M. M., I. B. and M. S.; writing – original draft: M. M., I. B., G. D. C., A. V. and F. T.; writing – review and editing: all authors.

Conflicts of interest

There are no conflicts to declare.

Data availability

The data supporting this article have been included in the paper and as part of the supplementary information (SI). Supplementary information is available. See DOI: https://doi.org/10.1039/d5dt02559a.

Acknowledgements

LP acknowledges funding by Funder: project funded by the European Union – NextGenerationEU under the National Recovery and Resilience Plan (NRRP), Mission 4 Component 2 Investment 1.3 – Call for tender No. 341 of 15.03.2022 of Ministero dell'Università e della Ricerca (MUR); Award number: project code PE0000021, Concession Decree No. 1561 of 11.10.2022 adopted by Ministero dell'Università e della Ricerca (MUR), CUP D43C22003090001, Project title "Network 4 Energy Sustainable Transition_NEST". The research was partially funded by University of Milan (Piano Sostegno alla Ricerca 2025 LINEA 2 grant: PSR2025_DIP_005_PI_DCARL).

References

1 W. Chen, J. Shen, Y. Huang, X. Liu and D. Astruc, Catalyzed Hydrolysis of Tetrahydroxydiboron by Graphene Quantum Dot-Stabilized Transition-Metal Nanoparticles for Hydrogen Evolution, *ACS Sustainable Chem. Eng.*, 2020, **8**, 7513–7522.
2 Z. Li and Q. Xu, Metal-Nanoparticle-Catalyzed Hydrogen Generation from Formic Acid, *Acc. Chem. Res.*, 2017, **50**, 1449–1458.
3 J. Yang, A. Sudik, C. Wolverton and D. J. Siegel, High capacity hydrogen storage materials: attributes for automotive applications and techniques for materials discovery, *Chem. Soc. Rev.*, 2010, **39**, 656–675.
4 C. Wang, Q. Wang, F. Fu and D. Astruc, Hydrogen Generation upon Nanocatalyzed Hydrolysis of Hydrogen-Rich Boron Derivatives: Recent Developments, *Acc. Chem. Res.*, 2020, **53**, 2483–2493.
5 M. Chandra and Q. Xu, A high-performance hydrogen generation system: Transition metal-catalyzed dissociation and hydrolysis of ammonia–borane, *J. Power Sources*, 2006, **156**, 190–194.
6 M. A. Khalily, H. Eren, S. Akbayrak, H. H. Susapto, N. Biyikli, S. Özkar and M. O. Guler, Facile Synthesis of Three-Dimensional Pt-TiO2 Nano-networks: A Highly Active Catalyst for the Hydrolytic Dehydrogenation of Ammonia–Borane, *Angew. Chem., Int. Ed.*, 2016, **55**, 12257–12261.
7 X. Yu, Z. Tang, D. Sun, L. Ouyang and M. Zhu, Recent advances and remaining challenges of nanostructured materials for hydrogen storage applications, *Prog. Mater. Sci.*, 2017, **88**, 1–48.
8 S. Akbayrak and S. Özkar, Magnetically Isolable Pt0/Co3O4 Nanocatalysts: Outstanding Catalytic Activity and High Reusability in Hydrolytic Dehydrogenation of Ammonia Borane, *ACS Appl. Mater. Interfaces*, 2021, **13**, 34341–34348.
9 S. Akbayrak, Y. Tonbul and S. Özkar, Magnetically Separable Rh0/Co3O4 Nanocatalyst Provides over a Million

Turnovers in Hydrogen Release from Ammonia Borane, *ACS Sustainable Chem. Eng.*, 2020, **8**, 4216–4224.

10 H. Wang, C. Gao, R. Li, Z. Peng, J. Yang, J. Gao, Y. Yang, S. Li, B. Li and Z. Liu, Ruthenium–Cobalt Nanoalloy Embedded within Hollow Carbon Spheres as a Bifunctionally Robust Catalyst for Hydrogen Generation from Water Splitting and Ammonia Borane Hydrolysis, *ACS Sustainable Chem. Eng.*, 2019, **7**, 18744–18752.

11 W. Chen, W. Zheng, J. Cao, W. Fu, G. Qian, D. Chen, X. Zhou and X. Duan, Atomic Insights into Robust Pt–PdO Interfacial Site-Boosted Hydrogen Generation, *ACS Catal.*, 2020, **10**, 11417–11429.

12 W. Gao, P. Wang, J. Guo, F. Chang, T. He, Q. Wang, G. Wu and P. Chen, Barium Hydride-Mediated Nitrogen Transfer and Hydrogenation for Ammonia Synthesis: A Case Study of Cobalt, *ACS Catal.*, 2017, **7**, 3654–3661.

13 Y. Wang, G. Shen, Y. Zhang, L. Pan, X. Zhang and J.-J. Zou, Visible-light-induced unbalanced charge on NiCoP/TiO2 sensitized system for rapid H2 generation from hydrolysis of ammonia borane, *Appl. Catal., B*, 2020, **260**, 118183.

14 W. Xu, W. Li, H. Wen, J. Ding, Y. Liu, W. Li and B. Li, Metal/metal-organic framework interfacial ensemble-induced dual site catalysis towards hydrogen generation, *Appl. Catal., B*, 2021, **286**, 119946.

15 R. Tahawy, E. Doustkhah, E.-S. A. Abdel-Aal, M. Esmat, F. E. Farghaly, H. El-Hosainy, N. Tsunoji, F. I. El-Hosiny, Y. Yamauchi, M. H. N. Assadi and Y. Ide, Exceptionally stable green rust, a mixed-valent iron-layered double hydroxide, as an efficient solar photocatalyst for H2 production from ammonia borane, *Appl. Catal., B*, 2021, **286**, 119854.

16 P. V. Ramachandran and P. D. Gagare, Preparation of Ammonia Borane in High Yield and Purity, Methanolysis, and Regeneration, *Inorg. Chem.*, 2007, **46**, 7810–7817.

17 D. Özhava, Y. Çiğdem and S. Ertürk, Methanolysis of ammonia borane catalyzed by magnetically isolable RHODIUM(0) nanoparticles, *Int. J. Hydrogen Energy*, 2023, **48**, 22942–22953.

18 D. Özhava and S. Özkar, Rhodium(0) nanoparticles supported on nanosilica: Highly active and long lived catalyst in hydrogen generation from the methanolysis of ammonia borane, *Appl. Catal., B*, 2016, **181**, 716–726.

19 D. Özhava and S. Özkar, Nanoceria supported rhodium(0) nanoparticles as catalyst for hydrogen generation from methanolysis of ammonia borane, *Appl. Catal., B*, 2018, **237**, 1012–1020.

20 L.-C. Liu, H.-L. Zhu and Y.-Q. Zheng, Defective Ehanced Subnano-Rh Catalyst Supported on an Ni@Ni-N-C Substrate for Highly Efficient Hydrolytic Dehydrogenation of Ammonia Borane, *ACS Appl. Energy Mater.*, 2022, **5**, 731–739.

21 Z. Zou, Y. Jiang and K. Song, Pd Nanoparticles Assembled on Metalporphyrin-Based Microporous Organic Polymer as Efficient Catalyst for Tandem Dehydrogenation of Ammonia Borane and Hydrogenation of Nitro Compounds, *Catal. Lett.*, 2020, **150**, 1277–1286.

22 N. Zhang, G. Liu, Y. Sun, Y. Wang, J. Yan and X. Liu, H2 Evolution Upon Hydrolysis of Ammonia-Borane Catalyzed by Porphyrin Stabilized Nanocatalysts, *Catal. Lett.*, 2021, **151**, 2272–2278.

23 X. Li, N. Yang, X. Cen, S. Li, L. Zhang and Z.-H. Lu, Exceptional activity of hollow porphyrin frameworks-confined Ni nanoparticles for hydrogen production from NaBH4 methanolysis, *Fuel*, 2023, **354**, 129332.

24 F. Limosani, H. Remita, P. Tagliatesta, E. M. Bauer, A. Leoni and M. Carbone, Functionalization of Gold Nanoparticles with Ru-Porphyrin and Their Selectivity in the Oligomerization of Alkynes, *Materials*, 2022, **15**, 1207.

25 J. Bonin, A. Maurin and M. Robert, Molecular catalysis of the electrochemical and photochemical reduction of CO2 with Fe and Co metal based complexes. Recent advances, *Coord. Chem. Rev.*, 2017, **334**, 184–198.

26 G. Di Carlo, M. Pizzotti, S. Righetto, A. Forni and F. Tessore, Electric-field-induced second harmonic generation nonlinear optic response of A4 β-pyrrolic-substituted ZnII porphyrins: When cubic contributions cannot be neglected, *Inorg. Chem.*, 2020, **59**, 7561–7570.

27 F. Limosani, F. Tessore, G. Di Carlo, A. Forni and P. Tagliatesta, Nonlinear optical properties of porphyrin, fullerene and ferrocene hybrid materials, *Materials*, 2021, **14**, 4404.

28 F. Limosani, F. Tessore, A. Forni, A. Lembo, G. Di Carlo, C. Albanese, S. Bellucci and P. Tagliatesta, Nonlinear Optical Properties of Zn(II) Porphyrin, Graphene Nanoplates, and Ferrocene Hybrid Materials, *Materials*, 2023, **16**, 5427.

29 S. Mathew, A. Yella, P. Gao, R. Humphry-Baker, B. F. E. Curchod, N. Ashari-Astani, I. Tavernelli, U. Rothlisberger, M. K. Nazeeruddin and M. Grätzel, Dye-sensitized solar cells with 13% efficiency achieved through the molecular engineering of porphyrin sensitizers, *Nat. Chem.*, 2014, **6**, 242–247.

30 L.-L. Li and E. W.-G. Diau, Porphyrin-sensitized solar cells, *Chem. Soc. Rev.*, 2013, **42**, 291–304.

31 A. Covezzi, A. O. Biroli, F. Tessore, A. Forni, D. Marinotto, P. Biagini, G. Di Carlo and M. Pizzotti, 4D-π-1A type β-substituted Zn-porphyrins: ideal green sensitizers for building-integrated photovoltaics, *Chem. Commun.*, 2016, **52**, 12642–12645.

32 G. Di Carlo, C. Albanese, A. Molinari, S. Carli, R. Argazzi, A. Minguzzi, F. Tessore, E. Marchini and S. Caramori, Perfluorinated Zinc Porphyrin Sensitized Photoelectrosynthetic Cells for Enhanced TEMPO-Mediated Benzyl Alcohol Oxidation, *ACS Appl. Mater. Interfaces*, 2024, **16**, 14864–14882.

33 S. Berardi, S. Caramori, E. Benazzi, N. Zabini, A. Niorettini, A. Orbelli Biroli, M. Pizzotti, F. Tessore and G. Di Carlo, Electronic Properties of Electron-Deficient Zn(II) Porphyrins for HBr Splitting, *Appl. Sci.*, 2019, **9**, 2739.

34 A. Orbelli Biroli, F. Tessore, G. Di Carlo, M. Pizzotti, E. Benazzi, F. Gentile, S. Berardi, C. A. Bignozzi, R. Argazzi, M. Natali, A. Sartorel and S. Caramori, Fluorinated ZnII

Porphyrins for Dye-Sensitized Aqueous Photoelectrosynthetic Cells, *ACS Appl. Mater. Interfaces*, 2019, **11**, 32895–32908.

35 S. J. Thompson, M. R. Brennan, S. Y. Lee and G. Dong, Synthesis and applications of rhodium porphyrin complexes, *Chem. Soc. Rev.*, 2018, **47**, 929–981.

36 B. B. Wayland, S. L. Van Voorhees and C. Wilker, Organometallic chemistry of rhodium tetraphenylporphyrin derivatives: formyl, hydroxymethyl, and alkyl complexes, *Inorg. Chem.*, 1986, **25**, 4039–4042.

37 X. Fu, S. Li and B. B. Wayland, Reactivity and Equilibrium Thermodynamic Studies of Rhodium Tetrakis(3,5-disulfonatomesityl)porphyrin Species with H2, CO, and Olefins in Water, *Inorg. Chem.*, 2006, **45**, 9884–9889.

38 X. Fu and B. B. Wayland, Thermodynamics of Rhodium Hydride Reactions with CO, Aldehydes, and Olefins in Water: Organo-Rhodium Porphyrin Bond Dissociation Free Energies, *J. Am. Chem. Soc.*, 2005, **127**, 16460–16467.

39 X. Fu and B. B. Wayland, Equilibrium Thermodynamic Studies in Water: Reactions of Dihydrogen with Rhodium (III) Porphyrins Relevant to Rh–Rh, Rh–H, and Rh–OH Bond Energetics, *J. Am. Chem. Soc.*, 2004, **126**, 2623–2631.

40 C. T. To and K. S. Chan, Selective Aliphatic Carbon–Carbon Bond Activation by Rhodium Porphyrin Complexes, *Acc. Chem. Res.*, 2017, **50**, 1702–1711.

41 C. T. To, K. S. Choi and K. S. Chan, Catalytic Carbon–Carbon σ-Bond Hydrogenation with Water Catalyzed by Rhodium Porphyrins, *J. Am. Chem. Soc.*, 2012, **134**, 11388–11391.

42 Y. Aoyama, T. Fujisawa, H. Toi and H. Ogoshi, Catalytic reactions of metalloporphyrins. 1. Catalytic modification of borane reduction of ketone with rhodium(III) porphyrin as catalyst, *J. Am. Chem. Soc.*, 1986, **108**, 943–947.

43 N. Tsolekile, V. Ncapayi, G. K. Obiyenwa, M. Matoetoe, S. Songca and O. S. Oluwafemi, Synthesis of meso-tetra-(4-sulfonatophenyl) porphyrin (TPPS4) – CuInS/ZnS quantum dots conjugate as an improved photosensitizer, *Int. J. Nanomed.*, 2019, **14**, 7065–7078.

44 M. Krishnamurthy, Kinetics of anation reactions of a water-soluble Rh(III)-porphyrin, *Inorg. Chim. Acta*, 1977, **25**, 215–218.

45 K. Anjali, N. J. Venkatesha, J. Christopher and A. Sakthivel, Rhodium porphyrin molecule-based catalysts for the hydrogenation of biomass derived levulinic acid to biofuel additive γ-valerolactone, *New J. Chem.*, 2020, **44**, 11064–11075.

46 T. Boschi, S. Licoccia and P. Tagliatesta, Novel rhodium porphyrin derivatives. II. Synthesis and characterization of hexacoordinated Rh(III) porphyrinates, *Inorg. Chim. Acta*, 1987, **126**, 157–160.

47 T. Boschi, S. Licoccia and P. Tagliatesta, Novel rhodium porphyrin derivatives. III. Synthesis and characterization of rhodium(III) porphyrinates in solution of alkyl amides, *Inorg. Chim. Acta*, 1988, **143**, 235–238.

48 T. Boschi, S. Licoccia and P. Tagliatesta, Novel rhodium porphyrin derivatives, *Inorg. Chim. Acta*, 1986, **119**, 191–194.

49 E. B. Fleischer, F. L. Dixon and R. Florian, The structure of bis(dimethylamine) α, β, γ, *δ*, -tetraphenyl-porphinerhodium (III) chloride, *Inorg. Nucl. Chem. Lett.*, 1973, **9**, 1303–1305.

50 W. Lai, M.-K. Lau, V. Chong, W.-T. Wong, W.-H. Leung and N.-T. Yu, The metal–carbon stretching frequencies in methyl complexes of Rh, Ir, Ga and In with porphyrins and a tetradentate pyridine–amide ligand, *J. Organomet. Chem.*, 2001, **634**, 61–68.

51 L. J. Boucher and J. J. Katz, The Infared Spectra of Metalloporphyrins (4000–160 Cm-1), *J. Am. Chem. Soc.*, 1967, **89**, 1340–1345.

52 G. G. Meng, B. R. James, K. A. Skov and M. Korbelik, Porphyrin chemistry pertaining to the design of anti-cancer drugs; part 2, the synthesis and in vitro tests of water-soluble porphyrins containing, in the meso positions, the functional groups: 4-methylpyridinium, or 4-sulfonatophenyl, in combination with phenyl, 4-pyridyl, 4-nitrophenyl, or 4-aminophenyl, *Can. J. Chem.*, 1994, **72**, 2447–2457.

53 K. Kalyanasundaram, Luminescence and triplet—triplet absorption spectra of rhodium(III) porphyrins, *Chem. Phys. Lett.*, 1984, **104**, 357–362.

54 M. Gouterman, G. H. Wagnière and L. C. Snyder, Spectra of porphyrins: Part II. Four orbital model, *J. Mol. Spectrosc.*, 1963, **11**, 108–127.

55 M. Gouterman, Spectra of porphyrins, *J. Mol. Spectrosc.*, 1961, **6**, 138–163.

56 V. Vasil'ev and I. V. Golovina, Behavior of Rhodium(III) Complexes with Water-soluble Porphyrins in Solutions, *Russ. J. Coord. Chem.*, 1998, **24**, 412–415.

57 S. Bellomi, D. C. Cano-Blanco, Y. Han, J. J. Delgado, X. Chen, K. A. Lomachenko, I. Barlocco, D. Ferri, A. Roldan and A. Villa, Understanding the interfacial changes of PtCo3O4 catalysts during the dehydrogenation of ammonia borane, *Appl. Surf. Sci.*, 2025, 164116.

58 M. A. Watzky and R. G. Finke, Transition metal nanocluster formation kinetic and mechanistic studies. A new mechanism when hydrogen is the reductant: slow, continuous nucleation and fast autocatalytic surface growth, *J. Am. Chem. Soc.*, 1997, **119**, 10382–10400.

59 S. Bellomi, D. C. Cano-Blanco, Y. Han, J. J. Delgado, X. Chen, K. A. Lomachenko, I. Barlocco, D. Ferri, A. Roldan and A. Villa, Understanding the interfacial changes of PtCo3O4 catalysts during the dehydrogenation of ammonia borane, *Appl. Surf. Sci.*, 2025, **711**, 164116.

60 R. Giovannetti, in *Macro To Nano Spectroscopy*, ed. J. Uddin, IntechOpen, Rijeka, 2012, DOI: 10.5772/38797.

61 S. Funahashi, Y. Inada and M. Inamo, Dynamic Study of Metal-Ion Incorporation into Porphyrins Based on the Dynamic Characterization of Metal Ions and on Sitting-Atop Complex Formation, *Anal. Sci.*, 2001, **17**, 917–927.

62 M. Roselló-Merino, R. J. Rama, J. Díez and S. Conejero, Catalytic dehydrocoupling of amine-boranes and amines into diaminoboranes: isolation of a Pt(ii), Shimoi-type, η1-BH complex, *Chem. Commun.*, 2016, **52**, 8389–8392.

63 L. Luconi, E. S. Osipova, G. Giambastiani, M. Peruzzini, A. Rossin, N. V. Belkova, O. A. Filippov, E. M. Titova,

A. A. Pavlov and E. S. Shubina, Amine Boranes Dehydrogenation Mediated by an Unsymmetrical Iridium Pincer Hydride: (PCN) vs (PCP) Improved Catalytic Performance, *Organometallics*, 2018, **37**, 3142–3153.

64 A. Telleria, P. W. N. M. van Leeuwen and Z. Freixa, Azobenzene-based ruthenium(II) catalysts for light-controlled hydrogen generation, *Dalton Trans.*, 2017, **46**, 3569–3578.